Journal of Zhejiang University-SCIENCE B (Biomedicine & Biotechnology) *2023 24(3):232-247*
www.jzus.zju.edu.cn; www.springer.com/journal/11585
E-mail: jzus_b@zju.edu.cn

Research Article

https://doi.org/10.1631/jzus.B2200351

AAZ2 induces mitochondrial-dependent apoptosis by targeting PDK1 in gastric cancer

Yi LI[1*], Wenyan SHE[2*], Xiaoran XU[1], Yixin LIU[1], Xinyu WANG[1], Sheng TIAN[1], Shiyi LI[1], Miao WANG[1], Chaochao YU[3], Pan LIU[1], Tianhe HUANG[1✉], Yongchang WEI[1✉]

[1]*Department of Radiation and Medical Oncology, Zhongnan Hospital of Wuhan University, Hubei Cancer Clinical Study Center & Hubei Key Laboratory of Tumor Biological Behaviors, Wuhan 430071, China*
[2]*College of Chemistry and Molecular Science, Wuhan University, Wuhan 430072, China*
[3]*Department of Integrated Chinese and Western Medicine, Zhongnan Hospital of Wuhan University, Wuhan University, Wuhan 430071, China*

Abstract: Drastic surges in intracellular reactive oxygen species (ROS) induce cell apoptosis, while most chemotherapy drugs lead to the accumulation of ROS. Here, we constructed an organic compound, arsenical *N*-(4-(1,3,2-dithiarsinan-2-yl)phenyl) acrylamide (AAZ2), which could prompt the ROS to trigger mitochondrial-dependent apoptosis in gastric cancer (GC). Mechanistically, by targeting pyruvate dehydrogenase kinase 1 (PDK1), AAZ2 caused metabolism alteration and the imbalance of redox homeostasis, followed by the inhibition of phosphoinositide-3-kinase (PI3K)/protein kinase B (AKT)/mammalian target of rapamycin (mTOR) pathway and leading to the activation of B-cell lymphoma 2 (Bcl2)/Bcl2-associated X (Bax)/caspase-9 (Cas9)/Cas3 cascades. Importantly, our in vivo data demonstrated that AAZ2 could inhibit the growth of GC xenograft. Overall, our data suggested that AAZ2 could contribute to metabolic abnormalities, leading to mitochondrial-dependent apoptosis by targeting PDK1 in GC.

Key words: *N*-(4-(1,3,2-dithiarsinan-2-yl)phenyl)acrylamide (AAZ2); Gastric cancer; Reactive oxygen species (ROS); Apoptosis; Pyruvate dehydrogenase kinase 1 (PDK1); Glucose metabolism

1 Introduction

Gastric cancer (GC) is one of the leading causes of cancer-related deaths worldwide (Smyth et al., 2020; Joshi and Badgwell, 2021). Our recent work discovered higher levels of reactive oxidative species (ROS) in GC patients, which initiate several signaling pathways to promote the development of GC (Gu et al., 2018). Mild ROS levels trigger the proliferation of cancer cells, while high ROS content leads to cell apoptosis (D'Souza et al., 2020; Harris and DeNicola, 2020). Thus, GC is potentially more vulnerable to oxidative stress-induced cell death when ROS-producing therapies are administered.

Aberrant energy metabolism usually causes an imbalance of redox homeostasis and ROS accumulation (Hayes et al., 2020), suggesting that targeting the energy metabolism pathway may be an effective antitumor strategy. Some chemotherapy drugs could interrupt glucose metabolism and subsequently promote ROS production, leading to cancer cell death (Hayes et al., 2020). The pyruvate dehydrogenase complex/pyruvate dehydrogenase (PDH) kinase (PDC/PDK) axis could induce a "glycolytic shift" and has long been recognized as an anti-cancer therapeutic candidate (Anwar et al., 2021). PDK1 can inhibit the activity of PDH through the phosphorylation of the E1α subunit (Anwar et al., 2021; Wang et al., 2022). Studies have shown that PDK inhibitors like dichloroacetate (DCA), monochloracetate (MCA), and sodium pyruvate have a biochemical half maximal inhibitory concentration (IC_{50}) value ranging from 10 to 100 μmol/L (Tataranni and Piccoli, 2019). Here, we speculated that acrylate (AA) and methacrylate (MAA) as pyruvate mimics could stimulate oxidative phosphorylation by inhibiting PDK1.

✉ Yongchang WEI, weiyongchang@whu.edu.cn
Tianhe HUANG, zn004593@whu.edu.cn
* The two authors contributed equally to this work
Yongchang WEI, https://orcid.org/0000-0001-7205-4663
Tianhe HUANG, https://orcid.org/0000-0002-2737-4016

Received July 1, 2022; Revision accepted Dec. 4, 2022;
Crosschecked Feb. 9, 2023

Arsenic trioxide (ATO, As_2O_3) is a compound that induces ROS production, causing oxidative stress, mitochondrial dysfunction, the activation of intracellular signaling pathways and DNA repair systems, and autophagy impairment (Sanz et al., 2019; Priya Wadgaonkar, 2021), which was demonstrated as effective in solid tumors, including lymphoma, GC, liver cancer, and pancreatic cancer (Wang QQ et al., 2020). Researchers are increasingly attempting to construct organic arsenicals to reduce the side effects of ATO. Notably, compared with inorganic arsenicals, organic arsenicals like darinaparsin (DAR) (Xu et al., 2019) and 4-(*N*-(*S*-glutathionylacetyl)amino) phenylarsonous acid (GSAO) (Elliott et al., 2012) have better structural diversity, stability, and bioavailability, and their clinical application value is increasingly appreciated. A phase II study found that DAR could be safely administered with tolerable toxicity profiles in advanced hepatocellular carcinoma (Wu et al., 2010). The anti-tumor effects of GSAO have been validated in a phase I trial (Elliott et al., 2012). In this work, we also generated an organic arsenical *N*-(4-(1,3,2-dithiarsinan-2-yl)phenyl) acrylamide (AAZ2) and showed that it could prompt ROS levels to trigger mitochondrial-dependent apoptosis in GC both in vivo and in vitro. Mechanistically, AAZ2 targeted PDK1, which triggered metabolism alteration and the imbalance of redox homeostasis, followed by the inhibition of phosphoinositide-3-kinase (PI3K)/protein kinase B (AKT)/mammalian target of rapamycin (mTOR) pathway, thus leading to the activation of B-cell lymphoma 2 (Bcl2)/Bcl2-associated X (Bax)/caspase-9 (Cas9)/Cas3 cascades.

2 Materials and methods

2.1 Cell culture and reagents

HGC-27 and AGS (human GC cell lines) were purchased from the Type Culture Collection of the Chinese Academy of Sciences (Shanghai, China). 293T and GES1 (cell lines) were gifts from Wuhan University. Cells were cultured in Roswell Park Memorial Institute (RPMI)-1640 (Gibco, Grand Island, NY, USA) medium containing 10% (volume fraction) fetal bovine serum (FBS; Gibco) with penicillin-streptomycin under 5% CO_2 at 37 °C.

ATO (202673) and *N*-acetylcysteine (NAC, 138061) were purchased from Sigma-Aldrich (St. Louis, MO, USA); benzyloxycarbonyl-Val-Ala-Asp-fluoromethylketone (Z-VAD-FMK, S7023) from Selleck (Houston, Texas, USA); insulin-like growth factor 1 (IGF1, 100-11) from Peprotech (Rocky Hill, NJ, USA); LY294002 (HY-10108) from MCE (NJ, USA); 2-deoxy-2-[(7-nitro-2,1,3-benzoxadiazol-4-yl)amino]-D-glucose (2-DGNB, 186689-07-6) from Cayman (Michigan, USA). The antibodies used were β-tubulin (10068-1-AP), mTOR (20657-1-AP), phosphorylated AKT (p-AKT, 66444-1-Ig), AKT (10176-2-AP), Bax (50599-2-Ig), Bcl2 (12789-1-AP), Cas3 (19677-1-AP), and Cas9 (10380-1-AP) from Proteintech (Wuhan, China); PDK1 (ab110025) from Abcam (Cambridge, MA, USA); p-PDH (AP1022) from ABclonal (Wuhan, China); poly(adenosine diphosphate (ADP)-ribose) polymerase (PARP, #9532) and cleaved-Cas3 (cle-Cas3, #9664) from the Cell Signaling Technology (Danvers, MA, USA); PDH (385512), p-PI3K (310163), p-mTOR (381557), cle-PARP (380374), and cle-Cas9 (381238) from ZEN-BIOIENCE (Chengdu, China); PI3K (AF6241) from Affinity (Sydney, AUS).

2.2 Synthesis and characterization of Z2 and AAZ2

4-(1,3,2-dithiarsinan-2-yl)aniline (Z2) is the precursor drug of AAZ2. The synthesis process of Z2 was as follows: *p*-arsanilic acid (5 g, 18.45 mmol) and 70% (volume fraction) ammonium thioglycolate (10 mL, 13 g, 120 mmol) were added into a 25-mL round flask containing a magnetic stir bar at 50 °C. After 4 h, 1,3-propanedithiol (4 mL, 23 mmol) was added dropwise and the mixture was stirred overnight. After the reaction completed, the mixture was extracted with dichloromethane (DCM). The organic layer was dried over anhydrous Na_2SO_4 and purified by column chromatography on silica gel (petroleum ether (PE)/DCM=1/4, volume ratio) to afford PAO-PDT in 50% yield. Subsequently, acyl chlorination was carried out to synthesize the final products.

For the synthesis process and characterization of AAZ2, a solution of Z2 (0.274 g, 1 mmol) in DCM (30 mL) was added to trimethylamine (TEA) (0.25 mL, 2 mmol) under N_2 atmosphere. After half an hour, acryloyl chloride was added dropwise at 0 °C followed by stirring for 2 h. The reaction mixture was quenched with H_2O and extracted with CH_2Cl_2 (3× 10 mL). The organic layer was washed with brine, dried over anhydrous Na_2SO_4, concentrated under reduced

pressure, and purified by column chromatography (PE/DCM=1/50, volume ratio) to afford AAZ2 as a white solid in 56% yield.

2.3 Cell viability assay

Cells were incubated in a 96-well plate overnight. After treated with AAZ2 (dissolved in dimethyl sulfoxide (DMSO), diluted in RPMI medium) for 24, 48, and 72 h, cholecystokinin-8 (CCK8) (Dojindo, Japan) was added followed by incubation, and the absorbance was read by a microplate reader (SpectraMax M2, Molecular Devices, USA).

2.4 Colony formation assay

Cells were incubated in six-well plates overnight, followed by 24 h of AAZ2 treatment. Next, cells were detached, centrifuged, re-counted, and re-plated, followed by 8 d of culture in normal culture medium. After washing with phosphate-buffered saline (PBS), methanol fixation, and 30 min of crystal violet staining, the colony numbers were calculated by ImageJ software (Schneider et al., 2012).

2.5 Determination of intracellular ROS accumulation

The treated samples were collected and stained with 10 μmol/L 2',7'-dichlorofluorescin diacetate (DCFH-DA; S0033S, Beyotime, China) or 5 μmol/L dihydroethidium (DHE) probe at 37 °C for 30 min. The ROS levels were finally determined by flow cytometry (BD, USA).

2.6 Analysis of cell apoptosis and cell cycle changes

Samples were harvested, washed, and stained with Annexin V/fluorescein isothiocyanate (FITC) and propidium iodide (PI) dye (CCS012, MultiSciences, China) for 5 to 10 min. The cell cycle was determined by staining with DNA staining and permeabilization solution. The final apoptotic rate and cell cycle distribution were detected using flow cytometry.

2.7 Transmission electron microscopy (TEM)

Samples treated and untreated with AAZ2 (0.8 μmol/L) were fixed with 2.5% (volume fraction) glutaraldehyde solution (G5882, Sigma-Aldrich) at 4 °C overnight. The dehydrated cells were embedded and stained with uranyl acetate. Representative areas were chosen from ultrathin sectioning and detected by TEM (Quantum Design, CA, USA).

2.8 Mitochondrial membrane potential (MMP) assay

Samples were stained with 5,5',6,6'-tetrachloro-1,1',3,3'-tetraethyl-imidacarbocyanine iodide (JC-1) dye (Cat#C2006, Beyotime) for 30 min, washed twice, and evaluated by flow cytometry.

2.9 Determination of lactic acid (LD) and adenosine triphosphate (ATP) production and glucose uptake level

Samples were harvested, disrupted, and centrifuged. Following the instructions of ATP detection kit (Cat# S0026, Beyotime), the supernatant and ATP working solution were incubated. Luminescence was measured by a microplate reader and quantified by relative light unit (RLU). The supernatants of the culture media were collected to evaluate the LD concentration following the detection kit (A019-2-1, Nanjing Jiancheng, China). As for glucose uptake capacity, cells were harvested and incubated with 100 mmol/L 2-DGNB (CAS186689-07-6, Cayman) for 30 min. Then, cells were washed, resuspended using glucose-free media, and detected by flow cytometry.

2.10 PDH activity

Samples were harvested and incubated with the reagents following the instructions of PDH reagent kit (PDH-1-Y, Suzhou Comin Biotechnology, China). The microplate reader (Molecular Devices) was used to detect PDK1 activity.

2.11 Molecular docking of AAZ2 to the PDK1 structural model

The simulation of docking interaction of AAZ2 and PDK1 was implemented using Schrödinger software (https://www.schrodinger.com). The protein crystal structure of PDK1 (PBD code: 2Q8F) originated from the RCSB Protein Data Bank (PDB) database (https://www.rcsb.org) and was prepared by removing water, adding hydrogens, and performing energy minimization through the Maestro 11.0 platform of Schrödinger. The structure of AAZ2 was transformed, with energy minimized in Chem3D module and optimized in Schrödinger. The glide docking mode was applied to dock the prepared ligand and receptor. The default parameters were used to run the docking simulation.

2.12 Simulation of molecular dynamics (MD)

The complex of PDK1 and AAZ2 was simulated by Desmond 2020 (https://www.schrodinger.com/

products/desmond). The third extended version of the optimized potentials for liquid simulations (OPLS3e) was chosen as the molecular force field, followed by energy minimization. Continuous systems were simulated by applying periodic boundary conditions. Long-range electrostatics were maintained by the particle mesh Ewald method. The system was equilibrated using an isothermal-isobaric ensemble (NPT) at a temperature of 300 K and a pressure of 1.0 bar (1 bar=0.1 MPa). The coupling of temperature-pressure parameters adopted the Berendsen coupling algorithm. The system ran for 100 ns at a time step of 1.2 fs. The track was recorded every 100 ps, and a total of 1000 frames were recorded.

2.13 Direct stochastic optical reconstruction microscopy (dSTORM) imaging

The treated and untreated samples were fixed with paraformaldehyde (15 min) and washed with PBS (three times). Next, cells were permeabilized with 0.2% (volume fraction) Triton X-100 (Sigma-Aldrich) for 10 min. After washing with PBS and blocking with 3% (volume fraction) bovine serum albumin (BSA; MCE) for 1 h, samples were incubated with primary antibody PDK1 at 4 °C overnight. The next day, samples were incubated with secondary antibodies for 40 min, followed by four times of washing with PBS.

Prior to imaging, cells were soaked in standard dSTORM buffer (50 mmol/L Tris, pH 8.0, 10 mmol/L NaCl, 10 % (0.1 g/mL) glucose, 100 mmol/L mercaptoethylamine, 500 μg/mL glucose oxidase, and 40 μg/mL catalase). Then, cells were imaged using 405 nm laser under the same power setting. The exposure time was 10 ms for both the fluorescence and bright field (BF) images. Finally, QC-STORM (Shang et al., 2021) was used to process the fluorescence images.

2.14 Western blot analysis

A total of 30 μg protein from each sample was separated by sodium dodecyl sulfate-polyacrylamide gel electrophoresis (SDS-PAGE; Shanghai Epizyme Biomedical Technology Co., Ltd., Shanghai, China) and transferred to a polyvinylidene fluoride (PVDF; Merck, Germany) membrane using wet transfer. After 60 min of blocking with 5% (0.05 g/mL) fat-free milk powder, the membrane was incubated with primary antibodies overnight at 4 °C. The next day, the samples were washed with PBS and incubated with secondary antibodies for 1 h at room temperature. The final immune complex was detected using an enhanced chemiluminescence (ECL) detection kit (Bio-Rad, NY, USA).

2.15 Quantitative polymerase chain reaction (qPCR)

Evo M-MLV RT Kit (Thermo Fisher, MA, USA) was used to synthesize complementary DNA (cDNA). qPCR was carried out in CFX96 real-time PCR detection systems (CFX96) with SYBR Green reagent (MCE). The $2^{-\Delta\Delta C_T}$ method was applied to calculate the relative expression level of PDK1 to β-tubulin (Table S1).

2.16 Cell transfections for gene silencing or overexpression

In order to knock down the expression of PDK1, small interfering RNA (siRNA) targeted for PDK1 (GenePharma, Shanghai, China) (Table S1) and negative control were transfected using Lipofectamine 3000 (Invitrogen, Carlsbad, CA, USA). The media needed to be replaced with fresh normal culture media 6–8 h later. After qPCR and western blot verification, cells could be used for subsequent experiments.

To overexpress PDK1, a CMVenhancer-MCS-polyA-EF1A-zs-Green-sv40-puromycin vector with PDK1 was inserted and an empty plasmid vector (Genechem, Shanghai, China) was transfected with Lipofectamine 3000 (Invitrogen) and P3000 reagent (Invitrogen).

2.17 RNA sequencing (RNA-seq)

Total RNA from samples was extracted using the Trizol reagent (15596026, Thermo Scientific, MA, USA) under strict quality control with RNA integrity number (RIN) values of 6.10–9.00. Subsequently, the ribosomal RNA (rRNA)-depletion method was selected to purify the samples, and RNA-seq libraries were constructed followed by an Illumina protocol (Illumina, San Diego, CA, USA). The Illumina HiSeq X Ten (PE150) platform was employed to sequence the libraries.

2.18 Immunohistochemistry (IHC) and staining with hematoxylin and eosin (HE)

The collected tumor tissues were fixed in 10% (volume fraction) formalin and embedded in paraffin. Specimens were sectioned at 5 μm thickness and stained using immunohistochemical techniques with primary antibodies against cle-Cas3 (1:100) and Ki67 (1:100). Secondary antibodies and diaminobenzidine

were used for detection. The organs were stained with HE for further observation.

2.19 Animals and treatments

Five-week-old female BALB/c nu/nu mice (18–22 g, n=21) were purchased from Vital River Laboratories (Beijing, China). The mice were randomly divided into three groups (n=7): vehicle, oxaliplatin (L-OHP), and AAZ2. A total of 4.5×10^6 HGC27 cells were injected into the right flank in 200 μL of serum-free RPMI-1640. When the average tumor volume reached about 100 mm^3, the mice were administered 10 mg/kg L-OHP, 10 mg/kg AAZ2, and vehicle every 5 d through intraperitoneal (i.p.) injection. The treatment duration lasted for 15 d. The tumor volume calculation formula was length×$width^2$×0.5. At the end of the study, all mice were sacrificed, and samples were harvested and processed for the subsequent assays.

2.20 Statistical analysis

Data from three independent experiments were presented as mean±standard deviation (SD). The GraphPad Prism 8.0 software (San Diego, USA) was applied for statistical analysis. When comparing more than two groups of data, one-way analysis of variance (ANOVA) followed by Dunnett's post-hoc test was used; when comparing multiple independent groups, one-way ANOVA and non-parametric Kruskal-Wallis test were performed followed by Dunnett's post-hoc test; when comparing two groups, unpaired Student's t-test was adopted. Statistical significance was defined as P-value of <0.05.

3 Results

3.1 Synthesis and cytotoxicity of AAZ2

We designed and synthesized three organic arsenicals: AAZ2, *N*-(4-(1,3,2-dithiarsinan-2-yl)phenyl)methacrylamide (MAZ2), and *N*-(4-(1,3,2-dithiarsinan-2-yl)phenyl)acetamide (ACZ2) (Fig. 1a). All of these compounds were characterized by nuclear magnetic resonance (NMR) spectroscopy and full-scan mass spectrometry (MS) (Fig. S1). AAZ2 was chosen as the candidate for its larger cytotoxicity to GC cells (Fig. 1b). The AGS and HGC27 were sensitive to AAZ2 (Fig. 1c). Thus, these two cell lines were selected for subsequent experiments. In addition, compared to the same concentration of ATO (the classical inorganic arsenic), AAZ2 was more cytotoxic to GC cells (Fig. 1d) and less cytotoxic to normal cells (Fig. 1e), including 293T and GES1. AAZ2 could also dramatically reduce the colony numbers (Figs. 1f and 1g) and induce G2/M phase arrest (Figs. 1h and 1i) in a dose-dependent manner.

3.2 Mitochondrial-dependent apoptosis induced by AAZ2 via ROS generation

Next, we attempted to explore the potential mechanism of AAZ2-induced cell death. Since ATO induced cell apoptosis through ROS accumulation, we first detected whether our organic arsenical AAZ2 could increase the intracellular ROS levels in GC cells. By means of DCFH-DA staining, we confirmed that AAZ2 could increase cellular ROS in a time- and dose-dependent manner (Fig. 2a), and ROS scavenger NAC could rescue ROS generation (Fig. 2b). Using TEM, the apoptotic bodies could be observed after AAZ2 treatment (Fig. 2c).

Since ROS play a significant role in determining mitochondrial-dependent apoptosis, we detected the effects of AAZ2 on the MMP and the mitochondrial-dependent apoptosis cascades. The flow cytometry results showed that AAZ2 treatment significantly decreased MMP, which could be attenuated by NAC, as shown by JC-1 staining (Fig. 2d). By means of Annexin V-FITC/PI staining, we also determined that AAZ2-induced apoptosis could be rescued by NAC (Fig. 2e).

Moreover, AAZ2 treatment altered the mitochondrial-mediated apoptotic pathways by upregulating the expression of cle-PARP, cle-Cas9, and cle-Cas3, and downregulating Bcl2 and Bax expression. Importantly, NAC could diminish the effect of AAZ2 on mitochondrial-mediated apoptotic pathways (Fig. 2f). Moreover, the pan-caspase inhibitor Z-VAD-FMK could attenuate AAZ2-induced apoptosis (Figs. 2g and 2h). Our data so far suggested that AAZ2 induced mitochondrial-dependent apoptosis via ROS generation.

3.3 ROS generation triggered by AAZ2 through targeting PDK1-mediated metabolism alteration

Later, we tried to figure out how AAZ2 promoted ROS generation. PDKs are major regulatory enzymes in glucose metabolism for their negative control of PDC by phosphorylation (Anwar et al., 2021), and AAZ2

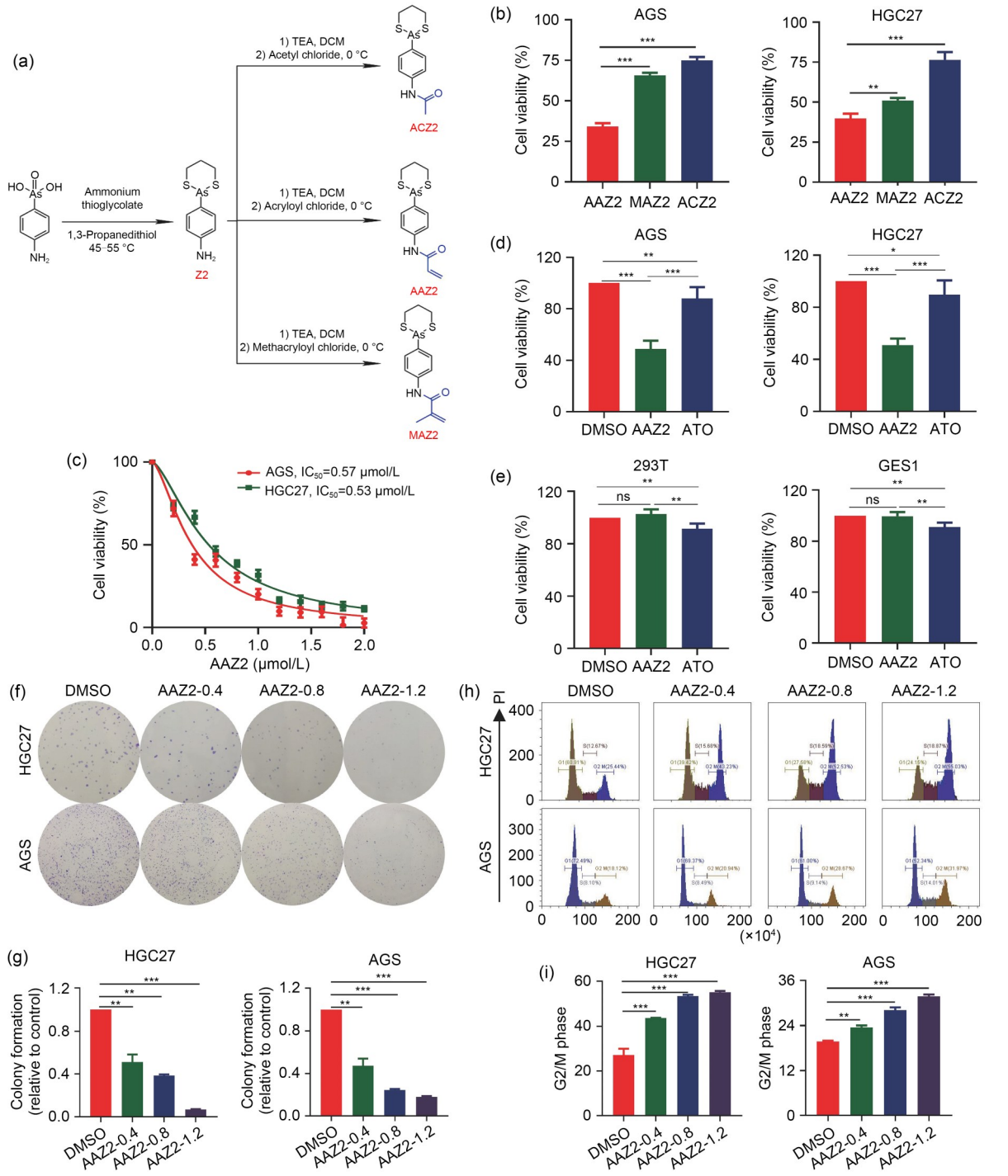

Fig. 1 Synthesis and cytotoxicity of AAZ2. (a) The synthesis process of AAZ2 compounds. (b) Viability of GC cells after exposure to AAZ2, MAZ2, and ACZ2 (1.0 μmol/L). (c) CCK8 used to evaluate the IC_{50} of GC cells after AAZ2 treatment for 48 h at various indicated concentrations. (d) Cell viability of GC cells under the same dose of AAZ2 and ATO (0.8 μmol/L). (e) Cell viability of normal cell lines 293T and GES1 under the same concentration of AAZ2 and ATO (0.8 μmol/L). (f) The colony formation ability evaluated upon AAZ2 exposure (0.4, 0.8, and 1.2 μmol/L). (g) Histogram of related colony numbers compared to the DMSO group. (h) Changes in the distribution of cell cycle detected following AAZ2 treatment. (i) Quantification of G2/M arrest rate. Data were presented as mean±standard deviation (SD), n=3. * P<0.05, ** P<0.01, *** P<0.001, and ns means no statistical significance. AAZ2: *N*-(4-(1,3,2-dithiarsinan-2-yl)phenyl)acrylamide; ACZ2: *N*-(4-(1,3,2-dithiarsinan-2-yl)phenyl)acetamide; ATO: arsenic trioxide; CCK8: cholecystokinin-8; DCM: dichloromethane; DMSO: dimethyl sulfoxide; GC: gastric cancer; IC_{50}: half maximal inhibitory concentration; MAZ2: *N*-(4-(1,3,2-dithiarsinan-2-yl) phenyl)methacrylamide;TEA: trimethylamine; Z2: 4-(1,3,2-dithiarsinan-2-yl)aniline.

was initially designed to target PDK1. Molecular simulation and molecular dynamics (MD) simulation were performed to verify the interaction between AAZ2 and PDK1. The docking models showed that AAZ2 could bind to PDK1 directly with a binding energy of −6.61 kcal/mol (Fig. 3a), which was better than the interaction between PDK1 and DCA (a commonly used PDK1 inhibitor) with a binding energy of −5.15 kcal/mol. Besides, MD simulation found that the root mean square deviation (RMSD) curve was less than 2.1 Å and

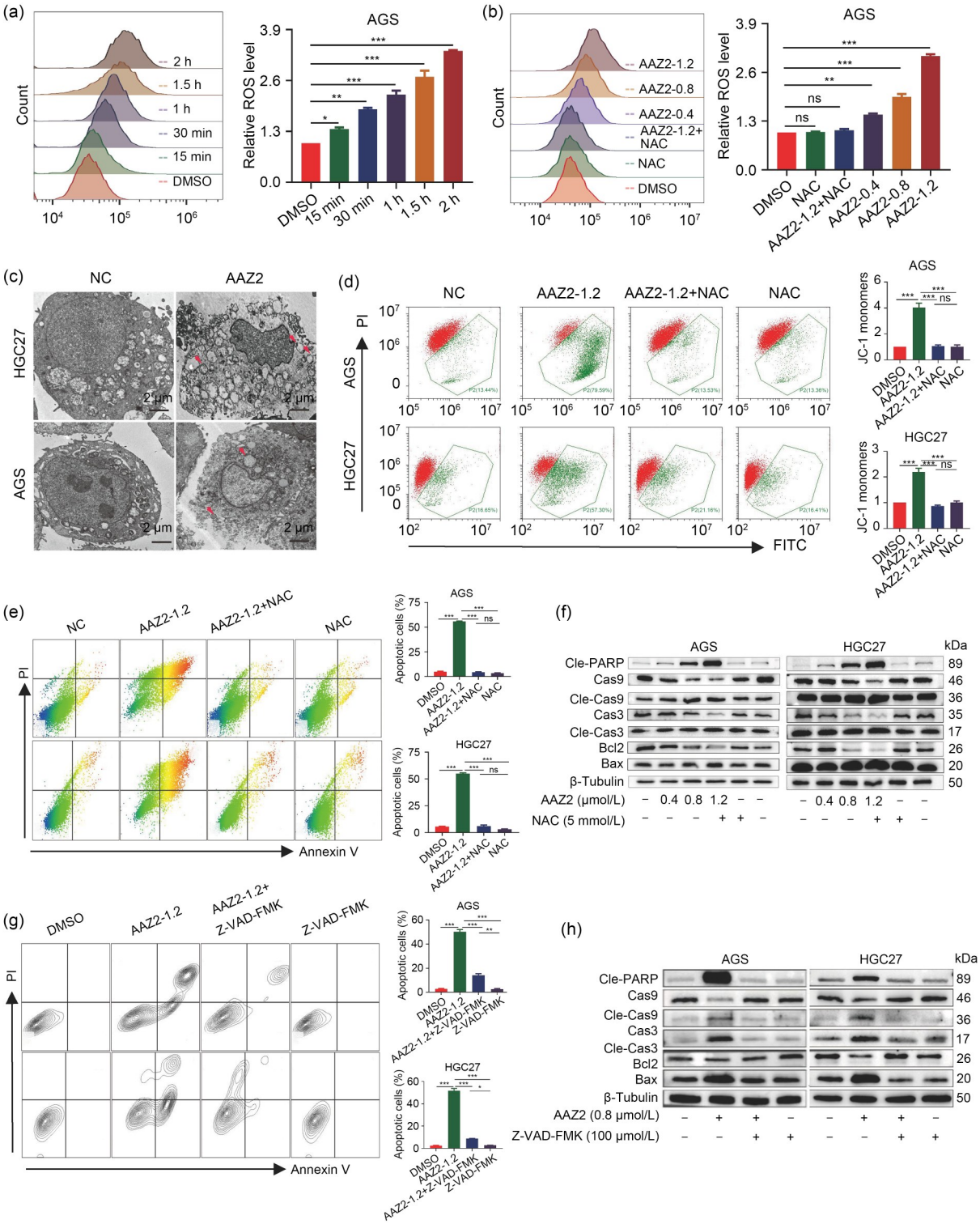

Fig. 2 Mitochondrial-dependent apoptosis induced by arsenical AAZ2 via ROS generation. (a) The ROS levels quantified using a DCFH-DA probe after different time of AAZ2 treatment (0.25, 0.5, 1, 1.5, and 2 h). (b) Quantification of ROS generation along with different doses of AAZ2 (0.4, 0.8, and 1.2 μmol/L) and NAC (5 mmol/L). (c) TEM images showing the apoptosis characteristics (0.8 μmol/L AAZ2). The red arrow refers to the apoptotic body. (d) Changes in the JC-1 monomers and aggregates determined by flow cytometry after AAZ2 (1.2 μmol/L) and NAC (5 mmol/L) treatments. (e) Apoptosis rates evaluated using flow cytometry after AAZ2 (1.2 μmol/L) and NAC (5 mmol/L) exposure. (f) The expression of apoptosis-related proteins analyzed by western blot. (g) Apoptosis rates evaluated using flow cytometry after Z-VAD-FMK (100 μmol/L) and AAZ2 (1.2 μmol/L) exposure. (h) Apoptosis-related proteins evaluated after exposure to pan-caspase inhibitor Z-VAD-FMK (100 μmol/L, 2 h pre-treatment) and AAZ2 (0.8 μmol/L). Data were presented as mean±standard deviation (SD), n=3. * P<0.05, ** P<0.01, *** P<0.001, and ns means no statistical significance. AAZ2: *N*-(4-(1,3,2-dithiarsinan-2-yl) phenyl)acrylamide; Bcl2: B-cell lymphoma 2; Bax: Bcl2-associated X; Cle-PARP: cleaved-poly(adenosine diphosphate (ADP)-ribose) polymerase; Cle-Cas9: cleaved-caspase-9; DCFH-DA: 2',7'-dichlorofluorescin diacetate; DMSO: dimethyl sulfoxide; FITC: fluorescein isothiocyanate; JC-1: 5, 5', 6, 6'-tetrachloro-1, 1', 3, 3'-tetraethyl-imidacarbocyanine iodide; NAC: *N*-acetylcysteine; NC: negative control; PI: propidium iodide; ROS: reactive oxygen species; TEM: transmission electron microscopy; Z-VAD-FMK: benzyloxycarbonyl-Val-Ala-Asp-fluoromethylketo (Note: for interpretation of the references to color in this figure legend, the reader is referred to the web version of this article).

reached dynamic equilibrium within 10 ns (Fig. 3b), demonstrating a robust and well-matched binding interaction between AAZ2 and PDK1. The western blot experiment verified that AAZ2 dramatically lowered the protein levels of PDK1, phosphorylated E1α subunit of PDH (p-PDH E1α) (Fig. 3c) and hypoxia-inducible factor-1α (HIF-1α) (Fig. S2a), and slightly increased the non-phosphorylated PDH E1α in a dose-dependent manner in GC cells (Fig. 3c). Using dSTORM, we discovered that the PDK1 density was 12.6–32.1 molecules/μm^2 before treatment and decreased to 9.4–28.8 molecules/μm^2 after 24 h of AAZ2 exposure (Figs. 3d and 3e). More importantly, AAZ2 treatment could increase the activity of PDH, which is downstream of PDK1 (Fig. 3f). These data advocated that PDK1 was a direct downstream target of AAZ2 in GC cells.

Given that the PDC/PDK axis can induce a "glycolytic shift," we next analyzed whether AAZ2 changed the metabolism of GC. It was found that AAZ2 could decrease glucose uptake, LD generation, and ATP level (Figs. 3g–3i), while lower AAZ2 levels (0.1 and 0.2 μmol/L) could rarely induce gastric cell death but could also induce this kind of shift (Figs. 2b–2d). These data indicated that AAZ2-mediated PDK inhibition contributed to the glucose metabolism shift from glycolysis and LD generation to glucose oxidation (Fig. 3j). Moreover, we tested the effects of ATO in GC cells. ATO failed to lead to a metabolic shift, as shown by the stable glucose uptake level and ATP and LD production (Figs. S2b–S2d). Correspondingly, ATO showed no effect on PDK1 (Fig. S2e) and PDH activity (Fig. S2f), suggesting that AAZ2 showed stronger antitumor effects than ATO, and that AAZ2 can function by targeting the specific target PDK1.

However, the relationship between ROS generation and AAZ2/PDK1-induced metabolism alteration remained to be explored. Thus, we built PDK1 overexpressing GC cells (Figs. 3k and 3l). Overexpression of PDK1 could reverse AAZ2-induced ROS generation (Fig. 3m), desensitize the GC to AAZ2 (Fig. 3n), and abate AAZ2-incuded apoptosis rates (Fig. 3o). Conversely, the knockdown of PDK1 (Figs. 3p and 3q) enhanced AAZ2-triggered ROS accumulation (Fig. 3r) and sensitized cells for the cytotoxic effect of AAZ2 (Figs. 3s and 3t). Taken together, our data supported that, by targeting PDK1, AAZ2 induced glycolytic phenotype alteration and subsequently led to ROS generation.

3.4 Mitochondrial-dependent apoptosis activated by AAZ2 through the inhibition of ROS-mediated PI3K/AKT/mTOR pathway

In order to better understand how ROS induce mitochondrial-dependent apoptosis, we performed RNA-seq for cells treated or untreated with AAZ2. AAZ2-treated cells showed a different gene profiling pattern (Fig. 4a). Gene set enrichment analysis (GSEA) demonstrated that differential genes mainly concentrated on apoptosis and glucose starvation (Fig. 4b). The PI3K/AKT/mTOR signaling pathway is one of the most well-known ROS-regulated pathways (Perillo et al., 2020), playing a vital role in tumor progression through proliferation enhancement, apoptosis inhibition, and glycolysis activation (Fattahi et al., 2020; Tewari et al., 2022). As expected, AAZ2 treatment decreased the protein levels of p-AKT, p-PI3K, and p-mTOR, and the inhibitory effects could be attenuated by NAC (Fig. 4c), suggesting that AAZ2/PDK1/ROS-induced cell apoptosis is mediated by the suppression of PI3K/AKT/mTOR pathways. In addition, the

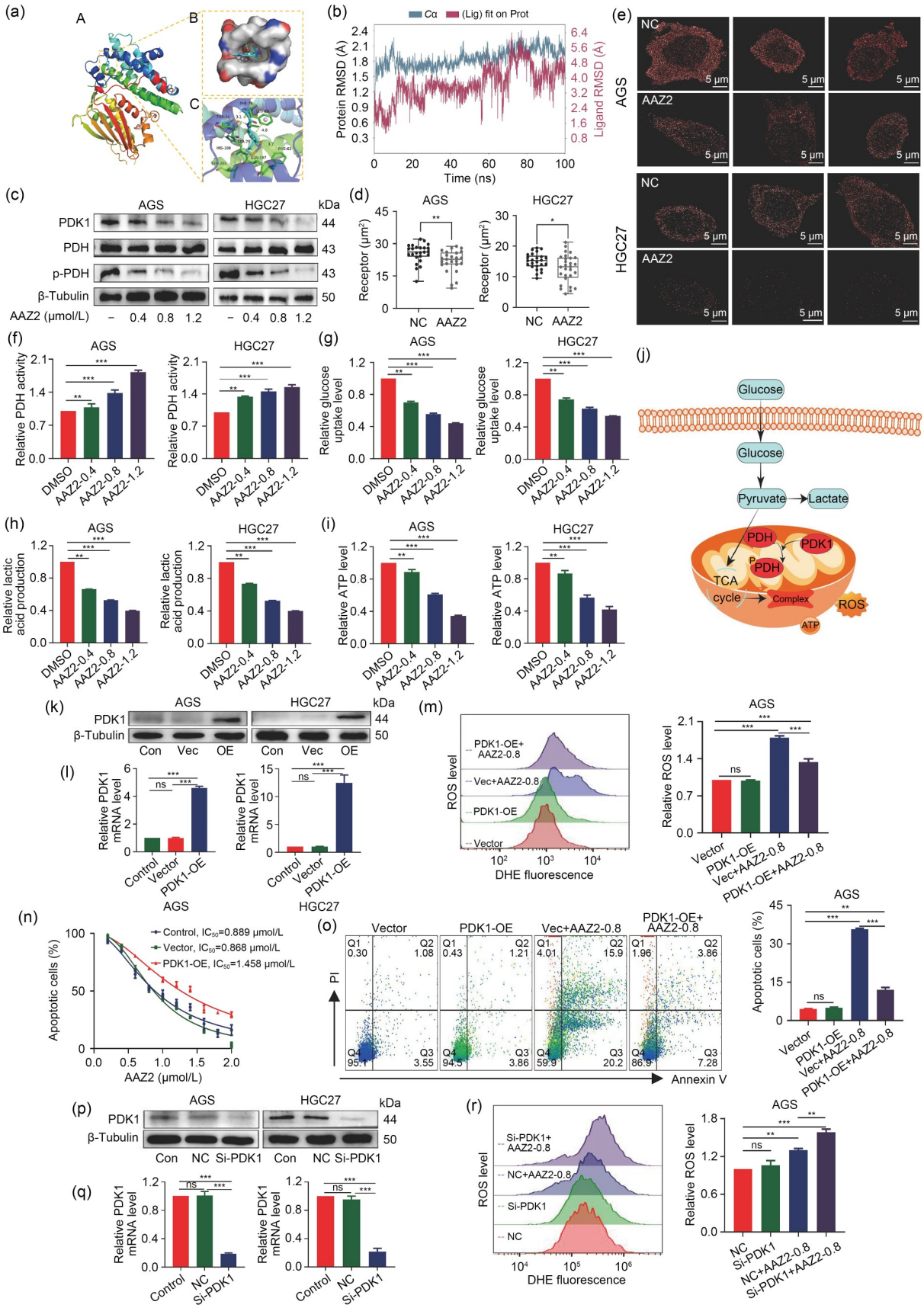
(a)
A
B
C
(b)
Cα
(Lig) fit on Prot
Protein RMSD (Å)
Ligand RMSD (Å)
Time (ns)
(c)
AGS
HGC27
kDa
PDK1
PDH
p-PDH
β-Tubulin
AAZ2 (μmol/L)
(d)
Receptor (μm²)
NC
AAZ2
(e)
NC
AAZ2
AGS
HGC27
5 μm
(f)
Relative PDH activity
DMSO
AAZ2-0.4
AAZ2-0.8
AAZ2-1.2
(g)
Relative glucose uptake level
(h)
Relative lactic acid production
(i)
Relative ATP level
(j)
Glucose
Pyruvate
Lactate
PDH
PDK1
TCA cycle
Complex
ROS
ATP
(k)
PDK1
β-Tubulin
Con
Vec
OE
(l)
Relative PDK1 mRNA level
Control
Vector
PDK1-OE
(m)
ROS level
PDK1-OE+ AAZ2-0.8
Vec+AAZ2-0.8
PDK1-OE
Vector
DHE fluorescence
Relative ROS level
(n)
Control, IC50=0.889 μmol/L
Vector, IC50=0.868 μmol/L
PDK1-OE, IC50=1.458 μmol/L
Apoptotic cells (%)
AAZ2 (μmol/L)
(o)
Vector
PDK1-OE
Vec+AAZ2-0.8
PDK1-OE+ AAZ2-0.8
PI
Annexin V
(p)
Con
NC
Si-PDK1
(q)
(r)
Si-PDK1+ AAZ2-0.8
NC+AAZ2-0.8
Si-PDK1
NC

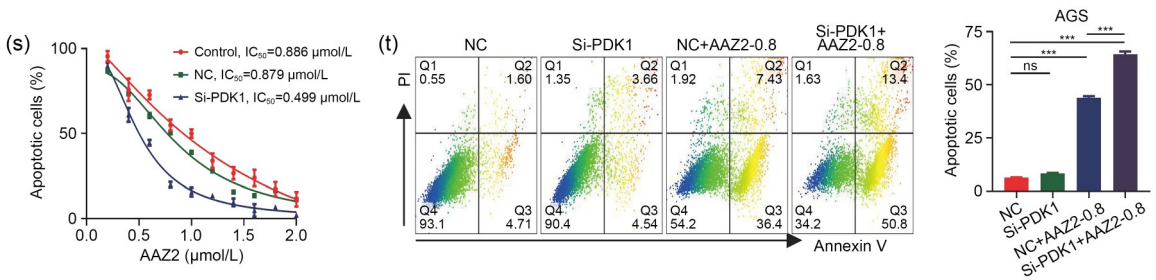

Fig. 3 ROS generation triggered by arsenical AAZ2 with targeting PDK1-mediated metabolism alteration. (a) Molecular docking between AAZ2 to the PDK1 structural model was simulated by Schrödinger software. (b) RMSD trajectories between AAZ2 and PDK1 using MD simulation within 100 ns. (c) The protein levels of PDK1, PDH, and p-PDH analyzed by western blot after AAZ2 treatment (0.4, 0.8, and 1.2 μmol/L). (d, e) PDK1 detected by dSTORM with or without AAZ2 treatment (0.8 μmol/L, 24 h); *n*=25. (f) PDH activity evaluated using the PDH reagent kit. (g–i) Detection of glucose uptake level and ATP and lactic acid production after AAZ2 exposure. (j) Schematic diagram of AAZ2-mediated glycolysis metabolic shifts. (k, l) Western blot and qPCR used for determining PDK1 expression in PDK1-overexpressing GC cells. (m) The ROS levels quantified using DCFH-DA probe in PDK1-overexpressing cells. (n) IC_{50} values of PDK1-overexpressing cells applied by CCK8. (o) Flow cytometry employed to evaluate the apoptosis rates of PDK1-overexpressing cells. (p, q) Western blot and qPCR used to verify the effect of knockdown of PDK1. (r) The ROS levels quantified using DCFH-DA probe in PDK1-knockdown cells. (s) The IC_{50} values of GC cells tested by CCK8 in PDK1-knockdown cells. (t) The apoptosis rates evaluated using flow cytometry. Data were presented as mean±standard deviation (SD), *n*=3. * *P*<0.05, ** *P*<0.01, *** *P*<0.001, and ns means no statistical significance. AAZ2: *N*-(4-(1,3,2-dithiarsinan-2-yl)phenyl) acrylamide; ATP: adenosine triphosphate; CCK8: cholecystokinin-8; Con: control; DCFH-DA: 2',7'-dichlorofluorescin diacetate; DHE: dihydroethidium; dSTORM: direct stochastic optical reconstruction microscopy; GC: gastric cancer; IC_{50}: half maximal inhibitory concentration; Lig: ligand; MD: molecular dynamics; mRNA: messenger RNA; NC: negative control; OE: over-expression; PDH: pyruvate dehydrogenase; PDK1: pyruvate dehydrogenase kinase 1; Prot: protein; p-PDH: phosphorylated PDH; qPCR: quantitative polymerase chain reaction; RMSD: root mean square deviation; ROS: reactive oxygen species; Si: knock-down; Vec: vector.

PI3K/AKT/mTOR pathway activator IGF1 and inhibitor LY294002 were used to test the specific effect of AAZ2. Pre-treatment with IGF1 slightly decreased the AAZ2-induced apoptosis (Figs. 4d and 4e) and increased cell viability (Fig. 4f). Correspondingly, the inhibitor LY294002 further enhanced apoptosis (Figs. 4g and 4h) and reduced cell viability (Fig. 4i). Collectively, we concluded that AAZ2/PDK1 induced the metabolism alteration and subsequent ROS accumulation, followed by suppressing the PI3K/AKT/mTOR signaling pathway to mediate mitochondrial-dependent apoptosis.

3.5 HGC27 xenograft growth inhibited by AAZ2 in vivo

The in vivo effect of AAZ2 on GC was determined using a HGC27 xenograft model (Fig. 5a). AAZ2 treatment could reduce both the volume and weight (Figs. 5b and 5c) of HGC27 xenograft tumors. No significant differences were detected in the body weight (Fig. 5d), hematological and biochemical parameters, including white blood cell (WBC), hemoglobin (HGB), platelet (PLT), alanine aminotransferase (ALT), aspartate aminotransferase (AST), creatinine, or urea nitrogen (Fig. 5e), as well as organ morphogenesis of liver, heart, and kidney (Fig. 5f) of mice, suggesting that AAZ2 had no significant side effects on nude mice. Consistent with the in vitro results, IHC staining indicated that AAZ2 decreased the expression level of Ki67 and increased that of cle-Cas3 (Fig. 5g). When using tumor tissue, we obtained similar trends as in vitro, including the change of PDK1 and mitochondrial-mediated apoptosis pathways (Fig. 5h). By analyzing the public dataset, we discovered that PDK1 was highly expressed in many cancers, including in GC. High levels of PDK1 in GC patients were positively correlated with poor overall survival (Figs. 5i and 5j). Thus, by targeting PDK1, AAZ2 showed promising anti-tumor activity with low toxicity to other organs and could be selected as a candidate reagent for cancer treatment.

4 Discussion

In this study, we constructed an organic arsenical, AAZ2, and demonstrated that it could prompt the ROS to trigger mitochondrial-dependent apoptosis in GC both in vitro and in vivo. By targeting PDK1, AAZ2

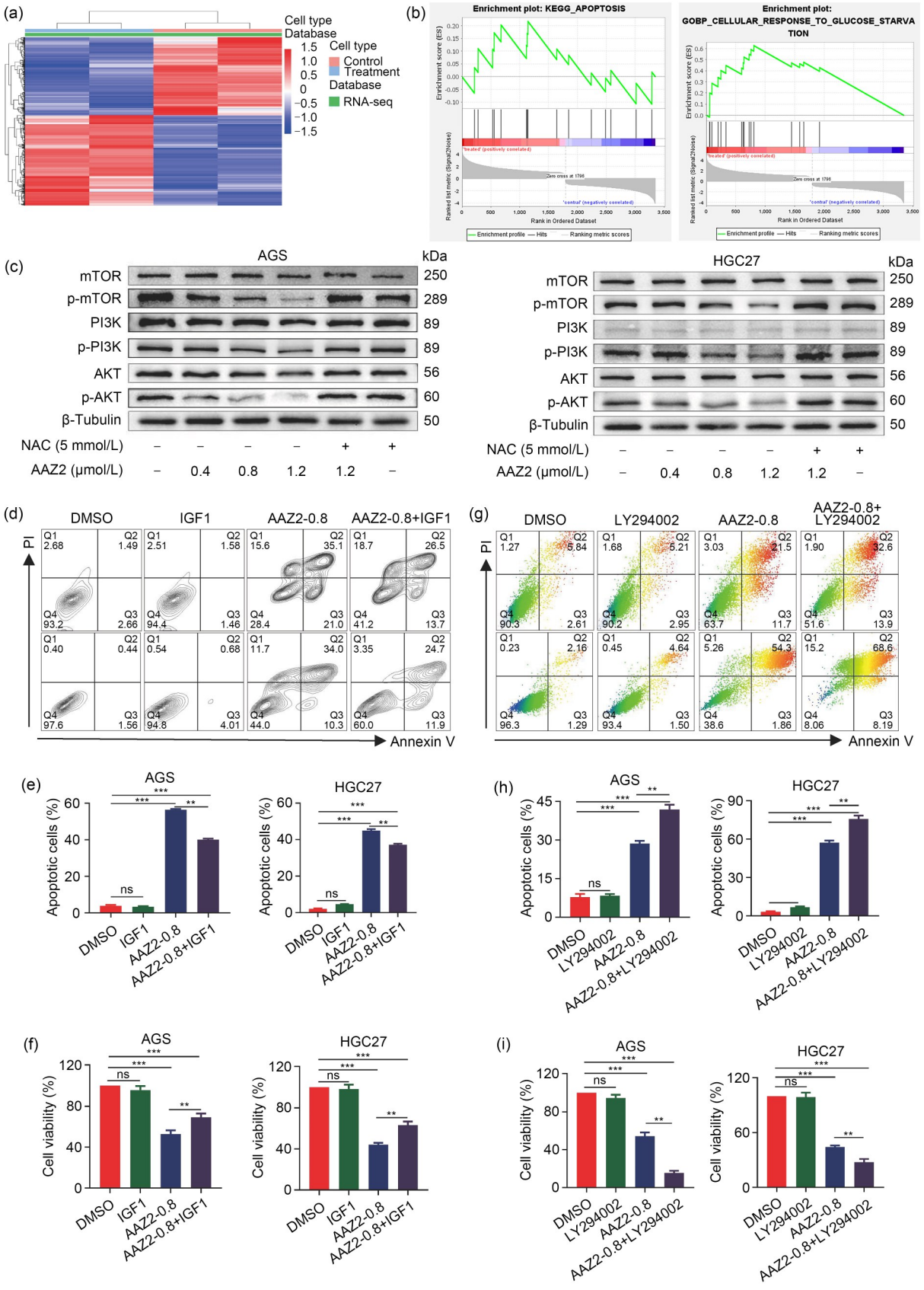
(a)
Cell type
Database
Cell type
Control
Treatment
Database
RNA-seq
(b)
Enrichment plot: KEGG_APOPTOSIS
Enrichment plot: GOBP_CELLULAR_RESPONSE_TO_GLUCOSE_STARVATION
(c)
AGS
HGC27
kDa
mTOR
p-mTOR
PI3K
p-PI3K
AKT
p-AKT
β-Tubulin
NAC (5 mmol/L)
AAZ2 (μmol/L)
(d)
DMSO
IGF1
AAZ2-0.8
AAZ2-0.8+IGF1
PI
Annexin V
(g)
DMSO
LY294002
AAZ2-0.8
AAZ2-0.8+LY294002
(e)
Apoptotic cells (%)
(h)
(f)
Cell viability (%)
(i)

Fig. 4 Mitochondrial-dependent apoptosis activated by arsenical AAZ2 through ROS-mediated inhibition of PI3K/AKT/mTOR pathway. (a) Differentially expressed genes identified after AAZ2 treatment. (b) GSEA results. (c) The protein levels of PI3K/AKT/mTOR pathway detected after AAZ2 (0.4, 0.8, and 1.2 μmol/L) and NAC (5 mmol/L) treatments. (d, e) Flow cytometry of cells exposed to pathway activator IGF1 (100 ng/mL, 2 h pre-treatment) and AAZ2 (0.8 μmol/L), and the apoptosis rates. (f) Cell viability of GC cells after the administration of IGF1 and AAZ2 (0.8 μmol/L). (g, h) Flow cytometry of cells pre-treated with pathway antagonists LY294002 (20 μmol/L, 2 h pre-treatment) and AAZ2 (0.8 μmol/L), and the apoptosis rates. (i) Cell viability of GC cells under exposure to LY294002 and AAZ2 (0.8 μmol/L). Data were presented as mean±standard deviation (SD), n=3. ** P<0.01, *** P<0.001, and ns means no statistical significance. AAZ2: *N*-(4-(1,3,2-dithiarsinan-2-yl)phenyl)acrylamide; AKT: protein kinase B; DMSO: dimethyl sulfoxide; GC: gastric cancer; GSEA: gene set enrichment analysis; IGF1: insulin-like growth factor 1; KEGG: Kyoto Encyclopedia of Genes and Genomes; mTOR: mammalian target of rapamycin; NAC: *N*-acetylcysteine; p-AKT: phosphorylated AKT; PI: propidium iodide; PI3K: phosphoinositide-3-kinase; RNA-seq: RNA sequencing; ROS: reactive oxygen species.

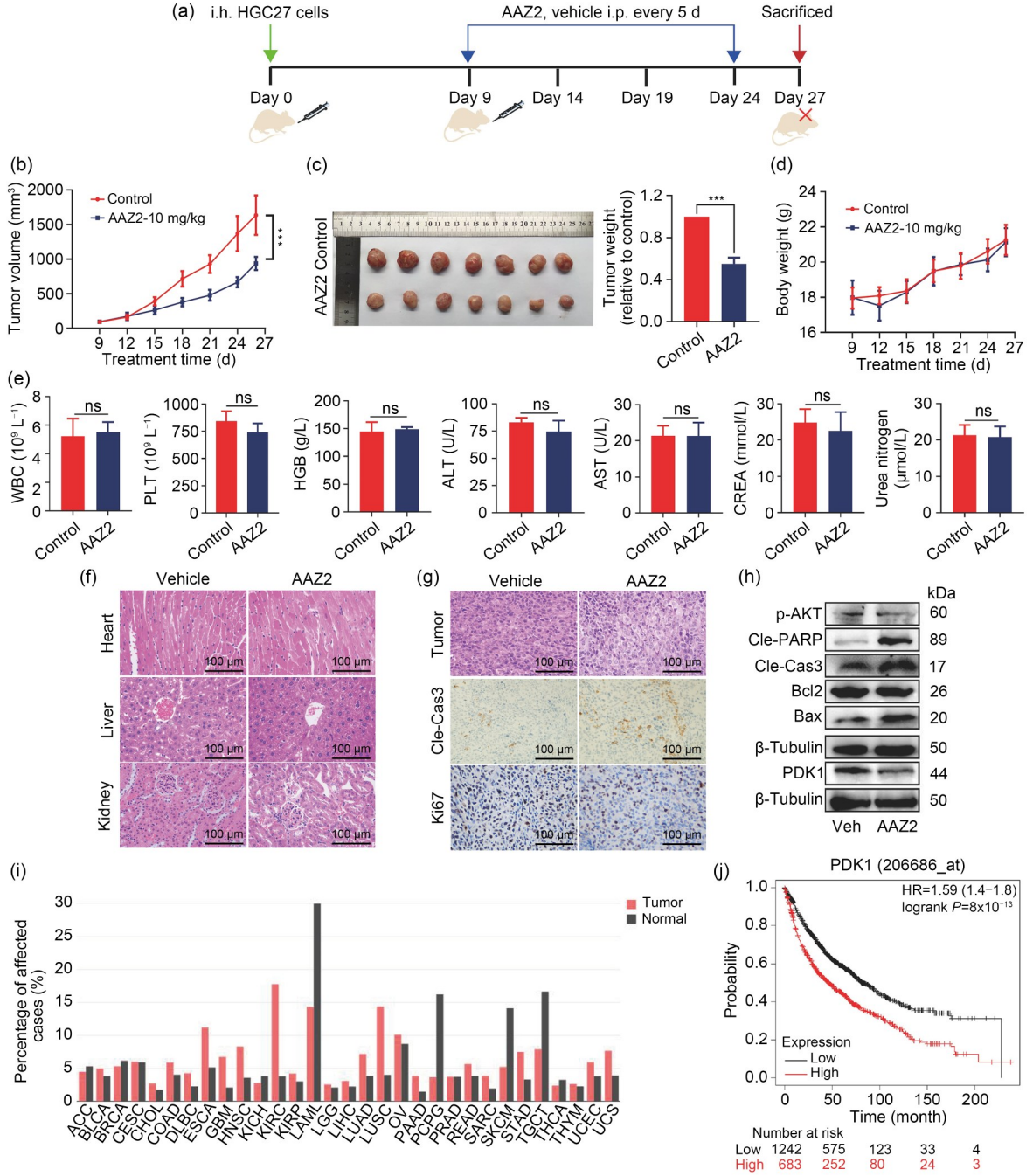

Fig. 5 HGC27 xenograft growth inhibited by arsenical AAZ2 in vivo, which demonstrated the clinical relevance. (a) Flowchart of animal experimental design. Changes in tumor volume (b), tumor weight (c), and body weight (d) with or without AAZ2 treatment (10 mg/kg). (e) Differences in the hematological and biochemical parameters between different treatment groups. (f) Representative images of HE staining in different organs (heart, liver, and kidney). (g) Representative images of tumor morphology (HE) and the expression of Ki67 and cle-Cas3 (IHC). (h) Western blot of analyzing pathway- and apoptosis-related protein levels. (i) Gene expression profiles across all tumor samples and paired normal tissues using data from the TCGA database. (j) High expression of PDK1 associated with poor survival based on Kaplan-Meier plotter. Data were presented as mean±standard deviation (SD), n=5. *** P<0.001 and ns means no statistical significance. AAZ2: *N*-(4-(1, 3, 2-dithiarsinan-2-yl)phenyl)acrylamide; ACC: adrenocortical carcinoma; ALT: alanine aminotransferase; AST: aspartate aminotransferase; Bcl2: B-cell lymphoma 2; Bax: Bcl2-associated X; BLCA: bladder urothelial carcinoma; BRCA: breast invasive carcinoma; CESC: cervical squamous cell carcinoma and endocervical adenocarcinoma; CHOL: cholangiocarcinoma; Cle-Cas3: cleaved-caspase-3; Cle-PARP: cleaved-poly(adenosine diphosphate (ADP)-ribose) polymerase; CREA: creatinine; COAD: colon adenocarcinoma; DLBC: lymphoid neoplasm diffuse large B-cell lymphoma; ESCA: esophageal carcinoma; GBM: glioblastoma multiforme; HE: hematoxylin and eosin; HGB: hemoglobin; HNSC: head and neck squamous cell carcinoma; HR: hazard ratio; IHC: immunohistochemistry; i. h.: hypodermic injection; i. p.: intraperitoneal; KICH: kidney chromophobe; KIRC: kidney renal clear cell carcinoma; KIRP: kidney renal papillary cell carcinoma; LAML: acute myeloid leukemia; LGG: brain lower grade glioma; LIHC: liver hepatocellular carcinoma; LUAD: lung adenocarcinoma; LUSC: lung squamous cell carcinoma; OV: ovarian serous cystadenocarcinoma; PAAD: pancreatic adenocarcinoma; p-AKT: phosphorylated protein kinase B; PCPG: pheochromocytoma and paraganglioma; PDK1: pyruvate dehydrogenase kinase 1; PLT: platelet; PRAD: prostate adenocarcinoma; READ: rectum adenocarcinoma; SARC: sarcoma; SKCM: skin cutaneous melanoma; STAD: stomach adenocarcinoma; TCGA: The Cancer Genome Atlas; TGCT: testicular germ cell tumor; THCA: thyroid carcinoma; THYM: thymoma; UCEC: uterine corpus endometrial carcinoma; UCS: uterine carcinosarcoma; WBC: white blood cell.

induced glycolytic phenotype alteration and subsequent ROS generation. Increased ROS suppressed the PI3K/AKT/mTOR signaling pathway, which induced mitochondrial-dependent apoptosis (Fig. 6).

PDK1 is highly expressed and associated with poorer overall survival in patients with GC (Lin et al., 2019). PDK1 has long been regarded as a potential therapeutic target that can negatively regulate PDC activity followed by the metabolic shift in cancer cells (Missiroli et al., 2020). Pai et al. (2021) reported that BX795, a PDK1 inhibitor, could enhance the efficacy of cisplatin and radiotherapy in oral squamous cell carcinoma. Anwar et al. (2021) demonstrated that the inhibition of PDK1 could lead to the removal of the glycolytic energy source and mandate the cancer cells for using mitochondrial resources, which induced toxic ROS and made cells prone to death signals. Here, docking and MD simulation showed a good binding capacity between PDK1 and AAZ2. Meanwhile, dSTORM, a single-molecule localization-based super-resolution microscopy (Nerreter et al., 2019; García-Guerrero et al., 2021), indicated that AAZ2 inhibited PDK1 expression in GC cells. AAZ2 also increased PDH activity and inhibited glucose metabolism. Furthermore, knockdown or overexpression of PDK1 could potentiate or attenuate the AAZ2-induced ROS generation and apoptosis, respectively. These data support that AAZ2 could inactivate PDK1, followed by glycolytic phenotype alteration and subsequent ROS generation. It is worth noting that AAZ2 could simultaneously decrease PDK1 expression and activity, indicating that inhibition is not the only mechanism by which AAZ2 reduces the PDK1 function. It has been reported that DCA (a classical PDK1 inhibitor) could reduce the protein levels of PDK1 in cancer cells (Velpula et al., 2013; Sradhanjali et al., 2017) and promote the degradation of HIF-1α, which in turn downregulated the expression of PDK1, suggesting a mechanism whereby DCA reduces the abundance of PDK1 via HIF-1α (Škorja Milić et al., 2021). Similar to DCA, AAZ2 is a pyruvate mimic and could inhibit the expression of HIF-1α (Fig. S2a). Excessive intracellular levels of ROS can damage the syntheses of lipids, proteins, and DNA, induce drug resistance (Cui et al., 2018), and even cause cell death, including autophagy and apoptosis (Weng et al., 2018; Perillo et al., 2020). Jin et al. (2020) reported that a PDK1 inhibitor, hemistepsin A, bound to the lipoamide-binding site of PDK1 and subsequently increased ROS generation and glycolysis inhibition, which induced ROS-dependent mitochondrial apoptotic both in vivo and in vitro. In this study, AAZ2 caused the accumulation of ROS as early as 15 min after AAZ2 treatment. Meanwhile, decreased MMP and increased apoptosis rates were observed, which could almost be attenuated by ROS scavengers NAC and Z-VAD-FMK, suggesting that AAZ2-mediated apoptosis was caspase-dependent in GC cells. Collectively, it can be reasonably concluded that AAZ2 exerts

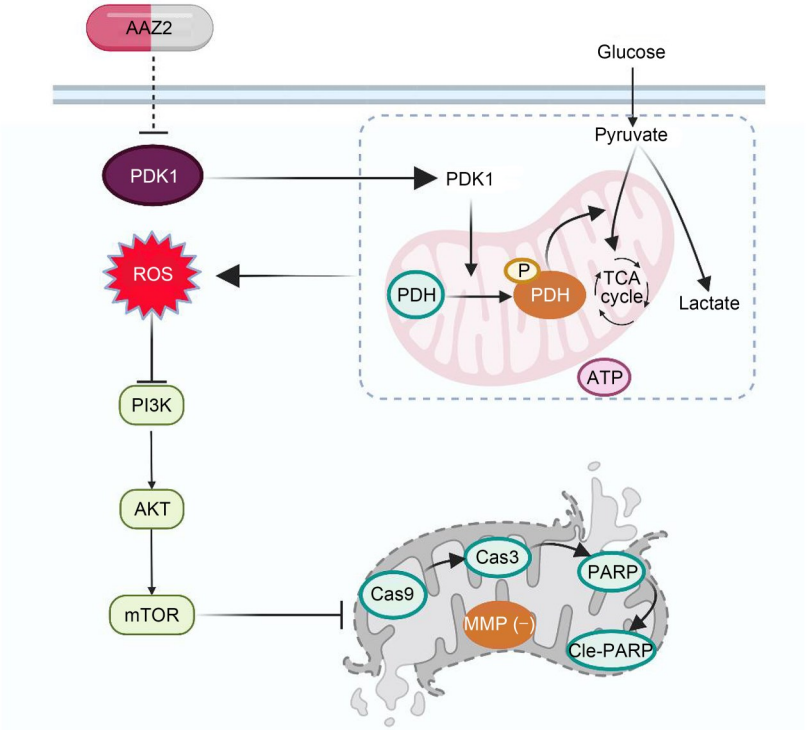

Fig. 6 Schematic diagram of the underlying mechanism of AAZ2-meditated anti-gastric cancer effects. AAZ2 caused the metabolism alteration and imbalance of redox homeostasis for ROS accumulation by targeting PDK1, inhibited the PI3K/AKT/mTOR pathway, and then led to the activation of Bcl2/Bax/Cas9/Cas3 cascades. AAZ2: *N*-(4-(1,3,2-dithiarsinan-2-yl)phenyl)acrylamide; AKT: protein kinase B; ATP: adenosine triphosphate; Bcl2: B-cell lymphoma 2; Bax: Bcl2-associated X; Cas9: caspase-9; Cle-PARP: cleaved-poly(adenosine diphosphate (ADP)-ribose) polymerase; MMP: mitochondrial membrane potential; mTOR: mammalian target of rapamycin; PDK1: pyruvate dehydrogenase kinase 1; PDH: pyruvate dehydrogenase; PI3K: phosphoinositide-3-kinase; ROS: reactive oxygen species; TCA: tricarboxylic acid cycle.

an anti-GC effect that is dependent on PDK1 inhibition and the subsequent accumulation of excessive ROS.

The PI3K/AKT/mTOR pathway is one of the major cellular signaling pathways that mediate essential intracellular functions and is tightly associated with ROS (Fattahi et al., 2020; Wang WP et al., 2020). In our study, RNA-seq suggested that differential genes were enriched in apoptosis and glucose starvation. Therefore, the PI3K/AKT/mTOR pathway was evaluated for AAZ2-mediated anti-GC effects. The western blot showed that AAZ2 could downregulate the levels of PI3K/AKT/mTOR pathway-related proteins. NAC could reverse the inhibitory effects, suggesting that ROS are involved in inhibiting the PI3K/AKT/mTOR pathway. The PI3K/AKT/mTOR pathway inhibitor LY294002 could potentiate AAZ2-mediated apoptosis, and activator IGF1 could partially attenuate apoptosis. All these data supported that ROS-mediated PI3K/AKT/mTOR pathway inhibition was involved in the process of AAZ2-mediated apoptosis.

5 Conclusions

In the present study, a novel organic arsenical, AAZ2, was constructed, which could inhibit the proliferation and growth of GC both in vitro and in vivo. By targeting PDK1, AAZ2 caused the metabolism alteration and imbalance of redox homeostasis, followed by the inhibition of PI3K/AKT/mTOR pathway, thus leading to the activation of mitochondrial-dependent apoptosis cascades. Therefore, AAZ2 may serve as a potential treatment agent for GC.

Acknowledgments

This study was supported by the Wuhan University Zhongnan Hospital Translational Medicine and Interdisciplinary Research Joint Fund (No. ZNJC201910), China.

Author contributions

Study design: Yi LI and Wenyan SHE; Data collection: Yi LI, Wenyan SHE, Xiaoran XU, Yixin LIU, Sheng TIAN, and

Shiyi LI; Data analysis: Yi LI, Yixin LIU, and Xinyu WANG; Data interpretation: Yi LI, Wenyan SHE, Xinyu WANG, and Miao WANG; Writing of manuscript: Yi LI; Critical revision: Yi LI, Chaochao YU, and Pan LIU; Final approval: Yi LI, Yongchang WEI, and Tianhe HUANG; Overall supervision: Tianhe HUANG and Yongchang WEI. All authors have read and approved the final manuscript, and therefore, have full access to all the data in the study and take responsibility for the integrity and security of the data.

Compliance with ethics guidelines

Yi LI, Wenyan SHE, Xiaoran XU, Yixin LIU, Xinyu WANG, Sheng TIAN, Shiyi LI, Miao WANG, Chaochao YU, Pan LIU, Tianhe HUANG, and Yongchang WEI declare that they have no conflict of interest.

The study was approved by the Medical Ethics Committee Zhongnan Hospital of Wuhan University (No. ZN2021006) and performed in accordance with the Declaration of Helsinki.

References

Anwar S, Shamsi A, Mohammad T, et al., 2021. Targeting pyruvate dehydrogenase kinase signaling in the development of effective cancer therapy. *Biochim Biophys Acta Rev Cancer*, 1876(1):188568. https://doi.org/10.1016/j.bbcan.2021.188568

Cui QB, Wang JQ, Assaraf YG, et al., 2018. Modulating ROS to overcome multidrug resistance in cancer. *Drug Resist Updat*, 41:1-25. https://doi.org/10.1016/j.drup.2018.11.001

D'Souza LC, Mishra S, Chakraborty A, et al., 2020. Oxidative stress and cancer development: are noncoding RNAs the missing links? *Antioxid Redox Signal*, 33(17):1209-1229. https://doi.org/10.1089/ars.2019.7987

Elliott MA, Ford SJ, Prasad E, et al., 2012. Pharmaceutical development of the novel arsenical based cancer therapeutic GSAO for Phase I clinical trial. *Int J Pharm*, 426(1-2): 67-75. https://doi.org/10.1016/j.ijpharm.2012.01.024

Fattahi S, Amjadi-Moheb F, Tabaripour R, et al., 2020. PI3K/AKT/mTOR signaling in gastric cancer: epigenetics and beyond. *Life Sci*, 262:118513. https://doi.org/10.1016/j.lfs.2020.118513

García-Guerrero E, Götz R, Doose S, et al., 2021. Upregulation of CD38 expression on multiple myeloma cells by novel HDAC6 inhibitors is a class effect and augments the efficacy of daratumumab. *Leukemia*, 35:201-214. https://doi.org/10.1038/s41375-020-0840-y

Gu HF, Huang TH, Shen YC, et al., 2018. Reactive oxygen species-mediated tumor microenvironment transformation: the mechanism of radioresistant gastric cancer. *Oxid Med Cell Longev*, 2018:5801209. https://doi.org/10.1155/2018/5801209

Harris IS, DeNicola GM, 2020. The complex interplay between antioxidants and ROS in cancer. *Trends Cell Biol*, 30(6): 440-451. https://doi.org/10.1016/j.tcb.2020.03.002

Hayes JD, Dinkova-Kostova AT, Tew KD, 2020. Oxidative stress in cancer. *Cancer Cell*, 38(2):167-197. https://doi.org/10.1016/j.ccell.2020.06.001

Jin L, Kim EY, Chung TW, et al., 2020. Hemistepsin A suppresses colorectal cancer growth through inhibiting pyruvate dehydrogenase kinase activity. *Sci Rep*, 10:21940. https://doi.org/10.1038/s41598-020-79019-1

Joshi SS, Badgwell BD, 2021. Current treatment and recent progress in gastric cancer. *CA Cancer J Clin*, 71(3):264-279. https://doi.org/10.3322/caac.21657

Lin JX, Xie XS, Weng XF, et al., 2019. UFM1 suppresses invasive activities of gastric cancer cells by attenuating the expression of PDK1 through PI3K/AKT signaling. *J Exp Clin Cancer Res*, 38:410. https://doi.org/10.1186/s13046-019-1416-4

Missiroli S, Perrone M, Genovese I, et al., 2020. Cancer metabolism and mitochondria: finding novel mechanisms to fight tumours. *eBioMedicine*, 59:102943. https://doi.org/10.1016/j.ebiom.2020.102943

Nerreter T, Letschert S, Götz R, et al., 2019. Super-resolution microscopy reveals ultra-low CD19 expression on myeloma cells that triggers elimination by CD19 CAR-T. *Nat Commun*, 10:3137. https://doi.org/10.1038/s41467-019-10948-w

Pai S, Yadav VK, Kuo KT, et al., 2021. PDK1 inhibitor BX795 improves cisplatin and radio-efficacy in oral squamous cell carcinoma by downregulating the PDK1/CD47/Akt-mediated glycolysis signaling pathway. *Int J Mol Sci*, 22(21):11492. https://doi.org/10.3390/ijms222111492

Perillo B, di Donato M, Pezone A, et al., 2020. ROS in cancer therapy: the bright side of the moon. *Exp Mol Med*, 52(2): 192-203. https://doi.org/10.1038/s12276-020-0384-2

Sanz MA, Fenaux P, Tallman MS, et al., 2019. Management of acute promyelocytic leukemia: updated recommendations from an expert panel of the European LeukemiaNet. *Blood*, 133(15):1630-1643. https://doi.org/10.1182/blood-2019-01-894980

Škorja Milić N, Dolinar K, Miš K, et al., 2021. Suppression of pyruvate dehydrogenase kinase by dichloroacetate in cancer and skeletal muscle cells is isoform specific and partially independent of HIF-1α. *Int J Mol Sci*, 22(16): 8610. https://doi.org/10.3390/ijms22168610

Smyth EC, Nilsson M, Grabsch HI, et al., 2020. Gastric cancer. *Lancet*, 396(10251):635-648. https://doi.org/10.1016/s0140-6736(20)31288-5

Sradhanjali S, Tripathy D, Rath S, et al., 2017. Overexpression of pyruvate dehydrogenase kinase 1 in retinoblastoma: a potential therapeutic opportunity for targeting vitreous seeds and hypoxic regions. *PLoS ONE*, 12(5):e0177744. https://doi.org/10.1371/journal.pone.0177744

Schneider CA, Rasband WS, Eliceiri KW, 2012. NIH Image to ImageJ: 25 years of image analysis. *Nat Methods*, 9(7): 671-675. https://doi.org/10.1038/nmeth.2089

Shang MT, Zhou ZW, Kuang WB, et al., 2021. High-precision 3D drift correction with differential phase contrast images. *Opt Express*, 29(21):34641-34655. https://doi.org/10.1364/OE.438160

Tataranni T, Piccoli C, 2019. Dichloroacetate (DCA) and cancer:

an overview towards clinical applications. *Oxid Med Cell Longev*, 2019:8201079. https://doi.org/10.1155/2019/8201079

Tewari D, Patni P, Bishayee A, et al., 2022. Natural products targeting the PI3K-Akt-mTOR signaling pathway in cancer: a novel therapeutic strategy. *Semin Cancer Biol*, 80:1-17. https://doi.org/10.1016/j.semcancer.2019.12.008

Velpula KK, Bhasin A, Asuthkar S, et al., 2013. Combined targeting of PDK1 and EGFR triggers regression of glioblastoma by reversing the Warburg effect. *Cancer Res*, 73(24): 7277-7289. https://doi.org/10.1158/0008-5472.can-13-1868

Wadgaonkar P, Chen F, 2021. Connections between endoplasmic reticulum stress-associated unfolded protein response, mitochondria, and autophagy in arsenic-induced carcinogenesis. *Semin Cancer Biol*, 76:258-266. https://doi.org/10.1016/j.semcancer.2021.04.004

Wang P, Jin JM, Liang XH, et al., 2022. Helichrysetin inhibits gastric cancer growth by targeting c-Myc/PDHK1 axis-mediated energy metabolism reprogramming. *Acta Pharmacol Sin*, 43(6):1581-1593. https://doi.org/10.1038/s41401-021-00750-0

Wang QQ, Jiang Y, Naranmandura H, 2020. Therapeutic strategy of arsenic trioxide in the fight against cancers and other diseases. *Metallomics*, 12(3):326-336. https://doi.org/10.1039/c9mt00308h

Wang WP, Dong XX, Liu Y, et al., 2020. Itraconazole exerts anti-liver cancer potential through the Wnt, PI3K/AKT/mTOR, and ROS pathways. *Biomed Pharmacother*, 131: 110661. https://doi.org/10.1016/j.biopha.2020.110661

Weng MS, Chang JH, Hung WY, et al., 2018. The interplay of reactive oxygen species and the epidermal growth factor receptor in tumor progression and drug resistance. *J Exp Clin Cancer Res*, 37:61. https://doi.org/10.1186/s13046-018-0728-0

Wu J, Henderson C, Feun L, et al., 2010. Phase II study of darinaparsin in patients with advanced hepatocellular carcinoma. *Invest New Drugs*, 28(5):670-676. https://doi.org/10.1007/s10637-009-9286-9

Xu XH, Wang HB, Li HY, et al., 2019. *S*-Dimethylarsinoglutathione (darinaparsin®) targets histone H3.3, leading to TRAIL-induced apoptosis in leukemia cells. *Chem Commun*, 55(87):13120-13123. https://doi.org/10.1039/c9cc07605k

Supplementary information

Table S1; Figs. S1 and S2